




Three-dimensional non-Abelian Bloch oscillations and higher-order topological states

Naiqiao Pan ^{1,2}, Tian Chen ^{1,2}✉, Tingting Ji¹, Xiaoxue Tong¹ & Xiangdong Zhang ¹✉

Recently, higher-order topological insulators (HOTIs) have been introduced, and were shown to host topological corner states under the theoretical framework of Benalcazar-Bernevig-Hughes. Here we unveil some topological effects in HOTIs by studying the three-dimensional (3D) non-Abelian Bloch oscillations (BOs). In HOTIs, BOs with a multiplied period occur when a force with a special direction is applied due to the effect of the non-Abelian Berry curvature. Along the direction of the oscillations we find a higher-order topological state that goes beyond the theoretical framework of multipole moments. The emergence of such a higher-order topological state coincides with the appearance of the 3D non-Abelian BOs. That is, the 3D non-Abelian BOs can be used as a tool to probe higher-order topological states. These phenomena are observed experimentally with designed electric circuit networks. Our work opens up a way to detect topological phases theoretically and experimentally.

¹Key Laboratory of advanced optoelectronic quantum architecture and measurements of Ministry of Education, Beijing Key Laboratory of Nanophotonics & Ultrafine Optoelectronic Systems, School of Physics, Beijing Institute of Technology, 100081 Beijing, China. ²These authors contributed equally: Naiqiao Pan, Tian Chen. ✉email: chentian@bit.edu.cn; zhangxd@bit.edu.cn

Topological phases exhibit some most striking phenomena in modern physics^{1,2}. Constructing new topological phases is very important in various physical systems because of their potential applications³⁻⁵. For example, constructing non-Abelian topological states is the basis of topological quantum computing^{6,7}. Topological phases can be characterized by different topological invariants⁸⁻¹⁰. Based on the bulk-boundary correspondence principle, the conventional topological phase is always featured by the boundary states with one-dimensional lower than the bulk that hosts them.

Recently, a novel class of the symmetry-protected higher-order topological insulator (HOTI) that possesses lower dimensional boundary states has been proposed¹¹ and realized in many systems, including mechanics¹², microwaves¹³, acoustics¹⁴⁻¹⁶, photonics¹⁷⁻²², solid materials²³, and electrical circuits^{24,25}. Comparing with conventional topological insulators of bulk dipole moments that lead to surface states, it is found that the unique boundary properties of HOTIs can be characterized by higher bulk multipole moments. For example, both of a quadrupole insulator in two dimensions and an octupole insulator in three dimensions manifests corner-bound states that are topologically protected, which can be discussed under the theoretical framework of Benalcazar-Bernevig-Hughes (BBH).

On the other hand, Bloch oscillations (BOs), in which a wavepacket undergoes a periodic motion in a lattice when subjected to a force²⁶⁻⁴², have emerged as a powerful tool for the detection of geometric and topological properties in synthetic lattice systems⁴³. This is because BOs are intrinsically related to the geometric and topological properties of the underlying band structure⁴⁴. Recently, two-dimensional (2D) non-Abelian BOs have been proposed theoretically in 2D HOTIs through the interplay of non-Abelian Berry curvature and quantized Wilson loops⁴⁵. Meanwhile, topologically protected edge states emerge on the open boundaries parallel to the body diagonals. The question is whether or not some new phenomena can occur in three-dimensional (3D) HOTIs through the interplay of non-Abelian Berry curvature and quantized Wilson loops.

In this work, we unveil some topological effects in the 3D HOTIs by studying 3D non-Abelian BOs. It is identified that a type of multiple BOs takes place along the diagonal of the body for the applied force, which is attributed to the finite non-Abelian Berry curvature of the degenerate band structure. Accompanied with these BOs there is a synchronized interband beating which is captured by the Wilson loop and can be topologically protected by winding numbers. Furthermore, higher-order boundary states appear at the symmetry axes associated with the topological BOs. Such edge states are localized on the one-dimensional boundary of the 3D system and cannot be characterized by the bulk octupole moments introduced by BBH. Furthermore, the wavepacket dynamics in the 3D HOTI model with an external force is realized theoretically and experimentally in a specially designed circuit network. The multiplying period of the topological BOs and the higher-order boundary states are also observed. Our results enrich the connection between topological BOs and non-Abelian systems, and expand the direction of exploring higher-order boundary states. Using the designed circuit network, our work paves the way for the experimental detection of wavepacket dynamics in complex lattice systems.

Results

The theory of topological BOs in 3D HOTIs. We consider a 3D lattice model consisting of cubic stacked unit cells, with each unit cell consisting of 8 lattice sites, as shown in Fig. 1a, b. These lattice

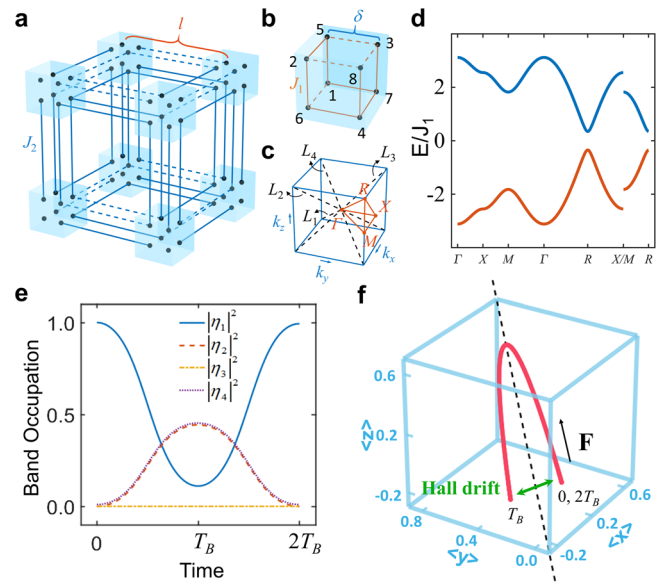


Fig. 1 Schematics and dynamics of the non-Abelian topological Bloch oscillations. **a** Tight binding model for the 3D higher-order topological insulator. Blue lines represent the intercell hopping amplitude of J_2 and dashed lines represent hopping terms with negative signs. The lattice constant is l . **b** One unit cell of the model where the sites are separated at an interval δ , with $\delta = 0.5l$. Red lines represent the intracell hopping amplitude of J_1 . **c** The first Brillouin zone with high-symmetry points highlighted. Black dashed lines along the body diagonals mark the four paths $L_1 - L_4$ exhibiting topological Bloch oscillations (BOs). **d** Band structure of the model. Each band is fourfold degenerate. **e** Band occupation dynamics along the L_1 path with an initial distribution $\eta(0) = (1, 0, 0, 0)^T$. Here $J_2 = 0.1J_1$ and the applied force satisfies $F_x = F_y = F_z = -0.2J_1$. **f** Real-space wavepacket trajectory of topological BOs indicated by the red curve. The black arrow indicates the direction of the applied force \mathbf{F} and the green double arrow shows the direction of the Hall drift. The trajectories of the first and second BOs coincide.

sites are distributed in space at equal intervals δ . As a result, the lattice constant takes $l = 2\delta$. The intracell and intercell hopping amplitudes are J_1 and J_2 respectively in all of the three spatial directions. In the discussion below, these 8 lattices in every unit cell have different spatial positions. Notice that if we ignore the geometric shape of the unit cell by setting the lattice sites in the center of the unit cell, the model is equivalent to the well-known BBH model¹¹. Taking $l = 1$, the model is represented by a Hamiltonian of the form:

$$H(\mathbf{k}) = \sum_{i=1}^6 d_i(\mathbf{k})\Gamma'_i, \tag{1}$$

where the operators $\Gamma'_i = -\sigma_2 \otimes \Gamma_i$ for $i = 1, 2, 3, 4, 5$, and $\Gamma'_6 = -\sigma_1 \otimes I_4$. Here, $\Gamma_1 = \sigma_0 \otimes \sigma_1$, $\Gamma_2 = \sigma_0 \otimes \sigma_2$, $\Gamma_3 = \sigma_1 \otimes \sigma_3$, $\Gamma_4 = -\sigma_2 \otimes \sigma_3$, $\Gamma_5 = \sigma_3 \otimes \sigma_3$, $I_4 = \sigma_0 \otimes \sigma_0$, and σ_i are Pauli matrices. The coefficients are expressed as $d_1(\mathbf{k}) = (J_1 - J_2) \sin(k_y/2)$, $d_2(\mathbf{k}) = -(J_1 + J_2) \cos(k_x/2)$, $d_3(\mathbf{k}) = (J_1 - J_2) \sin(k_x/2)$, $d_4(\mathbf{k}) = -(J_1 + J_2) \cos(k_x/2)$, $d_5(\mathbf{k}) = (J_1 - J_2) \sin(k_z/2)$, and $d_6(\mathbf{k}) = -(J_1 + J_2) \cos(k_z/2)$. The first Brillouin zone of the model with high-symmetry points highlighted is shown in Fig. 1c, the directions of the momentums k_x , k_y , and k_z are also marked. Four paths along the body diagonal directions of the BZ are illustrated as L_1 : $k_x = k_y = k_z$, L_2 : $-k_x = k_y = k_z$, L_3 : $k_x = -k_y = k_z$, and L_4 : $k_x = k_y = -k_z$, respectively. By solving the eigenfunction of the model $H|\psi\rangle = E|\psi\rangle$, we find that the model has two fourfold degenerate energy bands $E(\mathbf{k}) = \pm \epsilon(\mathbf{k}) = \pm \sqrt{3(J_1^2 + J_2^2)} + 2J_1J_2(\cos(k_x) + \cos(k_y) + \cos(k_z))$, which is shown in Fig. 1d. The fourfold

degeneracy of the energy bands comes from the three non-commuting mirror symmetries with respect to the x , y , and z directions, namely $M_x = \sigma_1 \otimes \sigma_1 \otimes \sigma_3$, $M_y = \sigma_1 \otimes \sigma_0 \otimes \sigma_1$, and $M_z = \sigma_1 \otimes \sigma_3 \otimes \sigma_3$, respectively.

We consider a wavepacket obtained as a superposition of the lowest four bands $|\psi_k^1\rangle$, $|\psi_k^2\rangle$, $|\psi_k^3\rangle$, and $|\psi_k^4\rangle$ (the full expressions of the bands are given in Supplementary note 1), and centered at \mathbf{k} , namely, $|\psi_k(t)\rangle = \eta_1(t)|\psi_k^1\rangle + \eta_2(t)|\psi_k^2\rangle + \eta_3(t)|\psi_k^3\rangle + \eta_4(t)|\psi_k^4\rangle$, with a distribution $\eta = (\eta_1, \eta_2, \eta_3, \eta_4)^T$, where $\sum_n |\eta_n|^2 = 1$. To study the dynamics of the wavepacket under the paths $L_1 \sim L_4$, we focus on the evolution of the state distribution according to:⁴⁶ $d\eta/dt = -i\varepsilon(\mathbf{k})\eta + i\mathbf{F}\cdot\mathbf{A}\eta$, where \mathbf{A} is the non-Abelian Berry connection whose matrix elements can be expressed as $A_i^{\alpha\beta} = i\langle\psi_k^\alpha|\partial_k|\psi_k^\beta\rangle$ with $\alpha, \beta = 1, 2, 3, 4$, and $\mathbf{F} = (F_x, F_y, F_z)$ is the applied force, which is homogeneous and constant that makes the momentum change linearly in time, $d\mathbf{k}/dt = \mathbf{F}$. We start with an initial state $|\psi_k(0)\rangle = |\psi_k^1\rangle$, which means $\mathbf{k}_0 = \Gamma$ and $\eta(0) = (1, 0, 0, 0)^T$. The applied force satisfies $F_x = F_y = F_z$ so that the moment moves along path L_1 in reciprocal space. Figure 1e displays the evolution of the four band occupations as a function of time. Here, T_B in the abscissa is the fundamental period of Bloch oscillations, namely $T_B = |\mathbf{G}_F|/|\mathbf{F}|$, with \mathbf{G}_F being the smallest reciprocal vector parallel to \mathbf{F} . Along the body diagonals, there is $T_B = 2\pi/|F_x|$ (we take the lattice constant as 1). We can see that in the first BO, the occupation of the first band $|\eta_1|^2$ decreases while $|\eta_2|^2$ and $|\eta_4|^2$ increase over time. In the second BO, $|\eta_1|^2$ increases while $|\eta_2|^2$ and $|\eta_4|^2$ decrease. Note that the occupation of the third band $|\eta_3|^2$ is always 0. After two BOs, the band occupations are brought back to their initial positions.

In fact, such dynamics of the wavepacket are topologically protected, which can be illustrated with a Wilson line matrix. The evolution of wavepacket can be formally solved as $\eta(t) = \exp(-i\int_0^t \varepsilon(\mathbf{k})dt)W\eta(0)$, where the Wilson line matrix W is defined as $W = \mathcal{P}\exp(i\int_{\mathbf{k}_0}^{\mathbf{k}_t} \mathbf{A}\cdot d\mathbf{k})$. Here, \mathcal{P} represents that the integral is path-ordered starting from \mathbf{k}_0 to the momentum at time t (\mathbf{k}_t). The Wilson line matrix intuitively exhibits the evolution of the degenerate bands under a specific path. The diagonal elements of this Wilson line matrix are the Berry connections of the individual bands, which produce the Berry phase when it is integrated along a closed path. The off-diagonal elements are the inter-band Berry connections which can bring about the inter-band transitions⁴⁵. When a force is applied along one of the body diagonal of the crystal, the Wilson line matrix under a closed path L_i ($i = 1, 2, 3, 4$) can be expressed as $W_{C_i} = \exp(i(\pi/2)w_i M_i)$, where M_i is a 4×4 matrix depending on the specific path (see Supplementary note 1 for the concrete expression), while $w_i = \pm 1$ is the novel winding number under the path L_i , which is defined as

$$w_i = \frac{i}{4\pi} \int_{L_i} d\mathbf{k} \cdot \text{Tr}[Q^{-1}(\mathbf{k})D_i\partial_{\mathbf{k}}Q(\mathbf{k})] \quad (2)$$

where $Q(\mathbf{k}) = i\sum_{i=1}^5 d_i(\mathbf{k})\Gamma_i - d_6(\mathbf{k})I_4$, and D_i is a 4×4 matrix depending on the path we choose (see Supplementary note 1 for details). Under the protection of a $2\pi/3$ rotation symmetry with the symmetry axis parallel to the specific path, Eq. (2) can be simplified as $w_i = \frac{1}{\pi} \int_0^{2\pi} d\mathbf{k} \frac{d_1\partial_k d_2 - d_2\partial_k d_1}{|\tilde{\mathbf{d}}|^2}$, where $\tilde{\mathbf{d}}(\mathbf{k}) = (d_1(\mathbf{k}), d_2(\mathbf{k}))$ (see Supplementary note 1 for details). As a result, the quantity w_i counts the number of times that the vector $\tilde{\mathbf{d}}(\mathbf{k})$ winds around the origin over the closed path L_i . For the $\tilde{\mathbf{d}}(\mathbf{k})$ provided in Eq. (1), $w_i = \text{sign}(J_1^2 - J_2^2) = \pm 1$. Thus, the winding number w_i is a topological invariant relating

to the band transitions protected by the crystalline symmetries. More demonstrations are also given in Supplementary note 1.

Based on the above results, we can further obtain that $W_{C_i}^2 = -I$, which means the wavepacket is brought back to itself when the momentum \mathbf{k} moves two reciprocal vectors along the path L_i . This is because the sign before the identity matrix and the trivial dynamical phase caused by the degeneracy of the bands do not influence the internal band-occupation dynamics. Such periodic dynamics of the wavepacket captured by the Wilson loop are topologically protected by winding numbers.

The phenomenon can also be verified by studying the real-space motion of the wavepacket. We consider the evolution of the real-space wavepacket $|\psi\rangle$ with an applied force \mathbf{F} . The evolution of the wavepacket can be obtained as the solution of the Schrödinger equation $i\partial_t\psi = H_B\psi$, as $|\psi(t)\rangle = e^{-iH_B t}|\psi(0)\rangle$, where $H_B = H + \mathbf{F}\cdot\mathbf{r}$. In a more common way, we describe the motion of the wavepacket using the semiclassical equation⁴⁶ $d\mathbf{r}/dt = \partial_{\mathbf{k}}\varepsilon(\mathbf{k}) - d\mathbf{k}/dt \times \eta^\dagger \mathbf{B}\eta$, where $\mathbf{B} = \nabla_{\mathbf{k}} \times \mathbf{A} - i\mathbf{A} \times \mathbf{A}$ denotes the non-Abelian Berry curvature. Note that the Hamiltonian $H(\mathbf{k})$ is diagonalized with fourfold degenerated conduction and valence bands. As studied in Ref. 47, the projection operators of conduction and valence bands can be expressed by a unit vector lying on a unit five-sphere S^5 , which is suitable for a 3D BBH model with specific parameters. In this way, the gauge group of the intra-band Berry connection and Berry curvature for BBH model corresponds to $SO(5)$. Figure 1f displays the evolution of the center of mass of the wavepacket according to the semiclassical equation, with the applied force satisfying $F_x = F_y = F_z = -0.4J_1$ and the initial distribution being $\eta(0) = (1, 0, 0, 0)^T$. It can be seen that the wavepacket experiences a transverse Hall drift perpendicular to \mathbf{F} after each BO, thus bringing the center of mass position back to its initial point after two BOs. This means that the evolution of the wavepacket has a period of $2T_B$. Such a behavior is synchronized and tightly connected with the band-population dynamics as shown in Fig. 1e. In the Methods section, we elucidate the synchronization with the help of the projected position operators under an atomic limit with $J_2 = 0$, and illustrate that such synchronization can only occur along the body diagonal directions and not in directions of other symmetry axes of this model. In fact, the periodic motion of the wavepacket can be directly obtained by analyzing the semiclassical equation. More discussions are given in Supplementary Note 2. The above results are focused on initial state $|\psi_k^1\rangle$. Evolution results under other initial states are provided in Supplementary Note 3. It should be added that the zero occupation of the third band in Fig. 1e is a combined effect of the external force and the band structure. While along other directions, this occupation is not vanishing, which is shown in Supplementary note 4.

Experimental observation of 3D topological BOs in electric circuits. As one of the most fundamental phenomena in solid-state physics, BOs were observed firstly in semiconductor superlattices^{26,27}. In the following decades, BOs have been observed in various physical systems, including ultracold atoms^{28,29}, Bose-Einstein condensates^{30,31}, and some classical wave systems³²⁻⁴². However, the experimental observation of the non-Abelian topological BOs keeps a challenge due to the strong anisotropy of the HOTI model. Recently, based on the similarity between circuit Laplacian and lattice Hamiltonian, simulating topological states with electric circuits has attracted lots of interest⁴⁸⁻⁶². Compared with other classical platforms, circuit

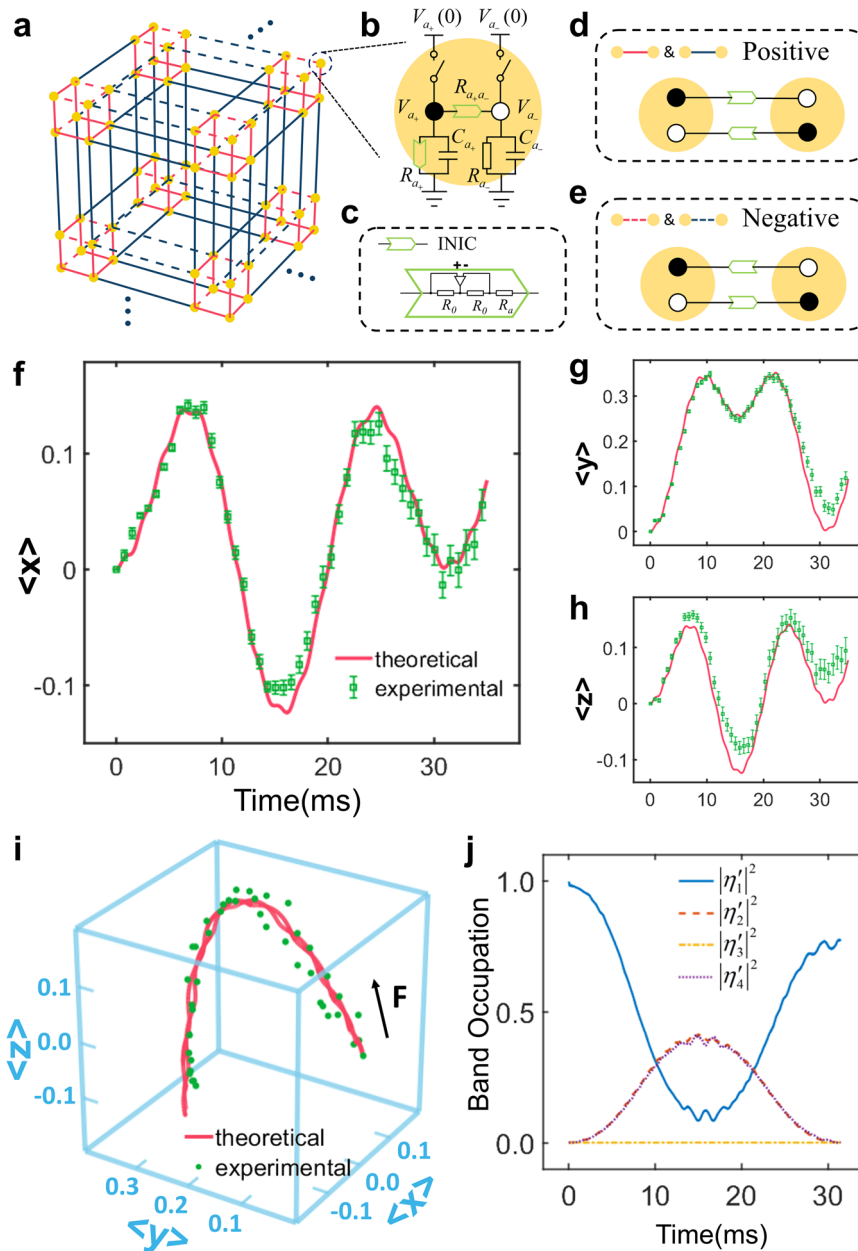


Fig. 2 Observation of the topological Bloch oscillations on electric circuits. **a** A schematic diagram of the designed circuit for the 3D higher-order topological insulator model with an applied force. **b** The internal structure of a circuit site with two nodes and their grounding parts. **c** The structure of the negative impedance converter with current inversion. **d, e** Connections between different sites for positive and negative hopping terms, respectively. **f-h** Simulation (red solid line) and experimental results (green dotted lines with error bars) for the center of mass of the circuit wavepacket in x , y , and z directions, respectively. The circuit is constructed for a lattice model with a finite size of $3 \times 3 \times 3$ unit cells and an applied force of $F_x = F_y = F_z = -0.4J_1$. Here $J_2 = 0.1J_1$ and J_1, J_2 are the intracell and intercell hopping amplitudes, respectively. The error bars are obtained from the average with data from 10 groups. **i** Simulation (red solid line) and experimental results (green dots) of real-space wavepacket trajectory. **j** Experimental results of Band occupation dynamics in momentum space.

networks possess remarkable advantages of being versatile and reconfigurable. Consequently, many extremely complex topological states are also fulfilled in circuit networks. In the following, we discuss experimental observation of 3D topological BOs with electric circuits.

Figure 2a illustrates the schematic diagram for the designed circuit corresponding to the lattice model in Fig. 1a with an applied force. Here, the red and blue lines represent the intracell and intercell hopping, respectively. Each yellow dot corresponds to an effective lattice site in the lattice model, and its internal

structure is shown in Fig. 2b. We use the voltages at nodes to simulate the real-space state in the lattice model. Since the components of the electronic state are complex and the circuit voltages are real, we use a circuit state $|\phi(t)\rangle = (V_{1+}(t), V_{2+}(t), \dots, V_{n+}(t), V_{1-}(t), V_{2-}(t), \dots, V_{n-}(t))^T$, which is combined of voltages of $2n$ nodes, to correspond to the real-space wavepacket with n sites. Here, V_{a+} and V_{a-} are the voltages at two nodes for the a -th site ($a = 1, \dots, n$), which are marked by the black and the white dots in Fig. 2b, respectively. These two

circuit nodes are connected through a negative impedance converter with current inversion (INIC) to realize the on-site potential. The structure of an INIC is illustrated in Fig. 2c, and its properties and functions are described in Ref. 51.

To simulate the hopping of the sites, two pairs of nodes are cross-connected via two INICs, the directions of which depend on the signs of the hopping amplitudes between the corresponding sites, as illustrated in Fig. 2d, e. Here, the effective resistances of the INICs are inversely proportional to corresponding parameters (on-site potentials and hopping amplitudes). Moreover, each node is grounded through a capacitor ($C_{a_{\pm}}$) parallel with an INIC or a normal resistor ($R_{a_{\pm}}$), as shown in Fig. 2b. More specific settings of the circuit are given in the Methods section. With the above settings, the evolution of circuit state $|\phi(t)\rangle$ can be expressed as a Schrödinger-like equation, $i\partial_t|\phi(t)\rangle = H_e|\phi(t)\rangle$, where H_e is the circuit Hamiltonian and has a form of $H_e = i\begin{pmatrix} O & -H_B' \\ H_B' & O \end{pmatrix}$, with H_B' corresponding to the real-space Hamiltonian H_B for the 3D lattice model. We define a circuit wavepacket $|\psi(t)\rangle$, which is a recombination of the circuit state, as $|\psi(t)\rangle = (v_1(t), v_2(t), \dots, v_n(t))^T$, where $v_a(t) = V_{a+}(t) - iV_{a-}(t)$. It can be confirmed that $|\psi(t)\rangle = e^{-iH_B't}|\psi(0)\rangle$, which corresponds to the evolution of the real-space wavepacket in the lattice model. A detailed demonstration is given in Methods section.

Now we numerically simulate the behavior of topological BOs to verify the effectiveness of our design. We construct a circuit system consisting of 216 pairs of nodes, which corresponds to an open-boundary lattice model consisting of $3\times 3\times 3$ unit cells with an applied force of $F_x = F_y = F_z = -0.4J_1$. Our system is small but still capable of demonstrating the topological BO phenomenon discussed above (see Supplementary Note 5 for details). Here, the grounding capacitances are all taken as $C_0 = 1 \mu\text{F}$. The effective resistances of the INICs corresponding to intracell and intercell hopping are set as 1 k Ω and 10 k Ω to realize the hopping amplitudes of $J_2 = 0.1J_1$, respectively. The effective resistance of the INIC between the node pair is set as $1/\mu$ to realize the corresponding on-site potential of μ . Furthermore, grounding INICs and resistors are also set appropriately. Under these parameter settings, the BO period for the circuit network is $T_B = 2\pi/|F_x| = 2\pi C_0 R_{J_1}/0.4 \approx 15.7\text{ms}$ theoretically. Here, R_{J_1} represents the effective resistance for intracell hopping, which is 1 k Ω .

To illustrate the BOs in our circuit system, we perform time-domain simulations of voltage dynamics using LTspice software. Figure 2f–h displays the evolution for the center of mass of the circuit wavepacket projected on three spatial directions of x , y , and z , respectively, marked by the red solid lines. Here, the abscissa is the actual evolution time of the simulated voltages, in milliseconds, and the ordinate is the spatial coordinate to the initial position. We set the initial state to be the same as $|\psi_1^1\rangle$ in all unit cells.

As shown in Fig. 2f–h, the center of mass along the x direction firstly goes through a rise and fall, and reaches a local minimum at about 16.1 ms, as well as in y and z directions, with the coordinates being $(-0.124, 0.254, -0.124)$. This indicates that the wavepacket completes an oscillation along the applied force \mathbf{F} , with the transverse displacement reaching the maximum. Then, the center of mass experiences another rise and fall in three directions, and reaches a local minimum which basically coincides with the origin, at about 30.9 ms. This reflects another oscillation with an opposite transverse drift bringing the center of mass back to its initial position. The spatial trajectory of the center of mass shown by the red curve

in Fig. 2i also illustrates this process, where the trajectories of the two BOs basically coincide. The simulated results clearly show that the period-two topological BOs take place in our circuit for the 3D HOTI system, with the period being ~ 30.9 ms, which is consistent with the theoretical result as $2T_B = 31.4$ ms.

Furthermore, we fabricate the corresponding circuit. A photograph image of the circuit sample is presented in Supplementary Note 6. We use the operational amplifier LT1013 and three surface-mounted device resistors to construct the INIC. All capacitors and resistors are manually selected within a tolerance of 1% to the theoretical values. More details about the experimental settings are given in Supplementary Note 6. The experimental results for the evolution of the wavepacket center of mass in three directions are shown by green dotted lines with error bars in Fig. 2f–h. The results are averaged by 10 repeated measurements. The spatial trajectory of the center of mass is also shown by the green dots in Fig. 2i. As can be seen, the center of mass experiences one BO in around 15.8 ms, bringing it to the position of $(-0.102, 0.247, -0.079)$. Then it goes through another BO that brings it back to $(-0.013, 0.057, 0.061)$ at about 30.8 ms. The experimental results match with the simulations well. We also notice that there is a slight deviation between the experimental and simulated results, which is a result of the voltages' dissipation caused by the disorder of circuit components and some other circuit losses. The detailed discussion is given in Supplementary Note 7.

The evolution of the band occupations can also be obtained by converting the real-space wavepacket into the momentum space through an inverse Fourier transform and calculating the occupations of the four degenerate bands $|\psi_k^1\rangle, |\psi_k^2\rangle, |\psi_k^3\rangle$ and $|\psi_k^4\rangle$. Figure 2j shows the experimental results for the evolution of the band occupations $|\eta'_1|^2, |\eta'_2|^2, |\eta'_3|^2$, and $|\eta'_4|^2$. As can be seen, the evolution corresponds to the theoretical prediction in Fig. 1e, ignoring a certain degree of attenuation. In all, the period-two topological BOs in 3D HOTI systems are successfully demonstrated through our designed circuit.

Higher-order boundary states. In addition to the period-multiplied topological BOs, we also discover that higher-order boundary states exist in the 3D HOTI system with specific edges. We consider a system with edges along the body diagonals of the original cubic lattice given in Fig. 1a, as shown in Fig. 3a. Here, the left part of Fig. 3a shows a schematic diagram of the original cubic stacked structure, with the blue lines indicating the directions of the open boundaries, and the right part of Fig. 3a illustrates the system with new boundaries. The complete structure of the unit cell is maintained on the boundaries, which is represented by the gray small cube in Fig. 3a. Furthermore, the intercell and intracell hopping amplitudes are the same as those given in Fig. 1a, b. We take x' , y' , and z' as the new spatial directions, where $\hat{z}' = \hat{x} + \hat{y} + \hat{z}$ is along the body diagonal while the x' and y' directions are the same as the previous x and y directions, respectively. If the periodic boundary conditions are taken along the z' direction, the calculated dispersion relations of the model are shown in Fig. 3, c. Here, 6 unit cells in both x' and y' directions are taken. Note that an extension of this mixed-boundary model has the same $2\pi/3$ rotation symmetry as the periodic system (see Supplementary Note 8).

When $J_1 > J_2$, there is no surface or hinge state in the complete band gap, indicating that this model is trivial, as shown in Fig. 3b. In contrast, when $J_1 < J_2$, the surface and hinge

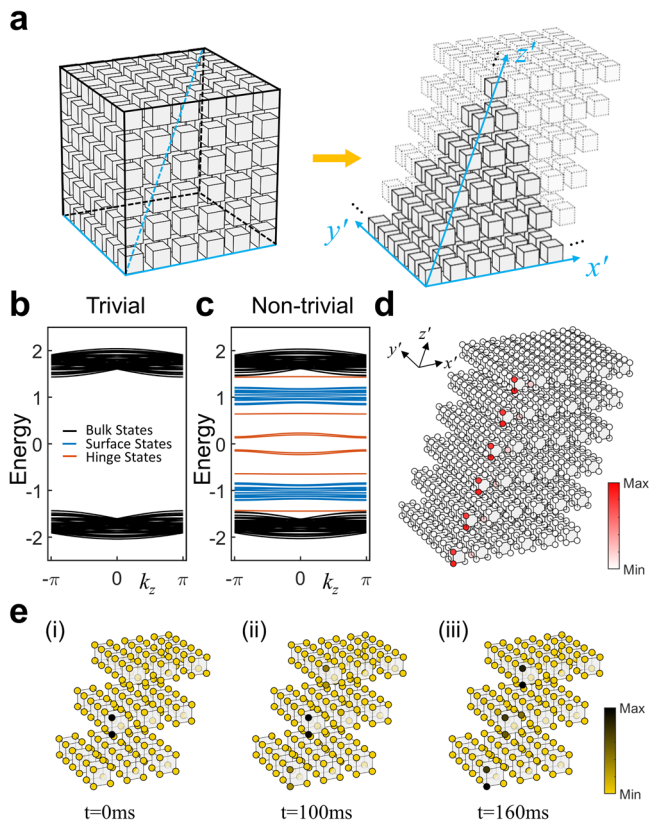


Fig. 3 Higher-order boundary states. **a** The system with edges along the body diagonal of the 3D higher-order topological insulator model. Here, the new spatial directions satisfy $\hat{z}' = \hat{x} + \hat{y} + \hat{z}$, $\hat{x}' = \hat{x}$, and $\hat{y}' = \hat{y}$. **b** Band structure of the system with periodic boundary conditions along the z' direction and finite sizes of 6 unit cells in x and y directions. It satisfies that $J_2 = 0.2J_1$, which is in a trivial phase. J_1, J_2 are the intracell and intercell hopping amplitudes, respectively. **c** Band structure of the system with $J_1 = 0.2J_2$, which is in a non-trivial phase. **d** An example of the higher-order boundary states which locates on the hinge of the model. **e** Experimental results that verify the boundary states with an electric circuit. The density of states indicated by the voltages at $t = 0$ ms, 100 ms, and 160 ms is displayed, which diffuses along the z' direction.

states can be observed in the band gap, as shown in Fig. 3c. For the surface states represented by blue bands in Fig. 3c, the electron density localizes at the surfaces of the model, except for the hinges, which is one dimension lower than the system (see Supplementary Note 9). As to the hinge states represented by red bands in Fig. 3c, it can be observed that the electron density concentrated along the hinges of the model but keeping the bulk and surfaces insulating, one example of which is shown in Fig. 3d. Such hinge states are two dimensions lower than the system, which are so called “higher-order” boundary states. We note that this kind of higher order boundary states does not exist in the 2D counterpart, since the edges along which the topological BOs take place are one dimension lower than the 2D system. Compared to the higher-order topological states exhibited in the initial BBH model, whose topological invariant is a bulk octupole moment captured by nested Wilson loops, the body diagonal edge states correspond to a vanishing nested Wilson loop invariant but are also topologically protected, which is indicated by the winding number w_i who changes the

sign when $J_1 = J_2$. In Supplementary Note 10, we explain such a phenomenon and give a proof of the topologically protected edge states.

To verify the higher-order boundary states, we also fabricate a corresponding circuit network consisting of $3 \times 3 \times 3$ unit cells with edges along the body diagonal. Compared to the parameters used in the circuits for topological BOs, the resistances of the INICs for intracell and intercell hopping are now set as 10 k Ω and 1 k Ω to realize the non-trivial hopping amplitudes of $J_1 = 0.1J_2$, and the connections of different sites are the same to those in Fig. 2d, e. Meanwhile, the real and imaginary nodes of the same site no longer need to be connected through an INIC, since we do not need an external force. Other parameters of the circuit components are also adjusted to appropriate values as needed. More details of the circuit structure and theoretical demonstration are given in Supplementary Note 11.

Now we excite the voltages at the nodes to observe the evolution of state on the outermost two sites of the cell located on the hinge at $t = 0$ ms, which is shown in Fig. 3e(i). The experimental results of the circuit wavepacket at $t = 100$ ms and 160 ms are displayed in Fig. 3e(ii) and 3e(iii). It can be seen that the electronic density of the state indicated by the circuit voltages diffuses along the z' direction within a finite time. Regardless of a small amount of voltage signals diffusing to the surface sites due to the influence of circuit disorders, most voltage signals occupy the outermost sites of the unit cells on hinge all the time, which indicates that the one-dimensional hinge state is a mode isolated from the bulk. The experimental result is a good demonstration of the existence of high-order boundary states, which is consistent with the theoretical expectations.

Discussion

We have demonstrated a type of period-multiplied BOs that takes place in the 3D HOTI model. Under an applied force along the body diagonals, the degenerate bands experience periodic inter-band transitions captured by Wilson loops, which are topologically protected by winding numbers. The corresponding dynamics of the real space center of mass of the wavepacket has also been observed, which is attributed to the finite non-Abelian Berry curvature of the degenerate band structure. Furthermore, higher-order boundary states have been shown to be exist on specific boundaries, which cannot be characterized under the framework of multipole moments. However, the emergence of such a higher-order topological state coincides with the appearance of the 3D non-Abelian BOs. This means that the higher-order topological states can be probed by 3D non-Abelian BOs. With the help of a specific designed circuit network which exactly maps the lattice model, we have successfully demonstrated the above theories. The period-multiplied topological BOs have not only been observed experimentally in the 3D circuit lattices through the time-dependent evolution of the voltages, but also the higher-order boundary states have been verified in the circuit system.

Preceding our work, ref. 47. has identified 1D, 2D, and 3D topological invariants for characterizing higher order topological insulators and demonstrate the existence of gapless spectra of Wilson loops and surface-states along the body diagonal directions of the Brillouin zone of BBH models, which deserves attention. Besides, related works on topological classification through crystal symmetries and Wilson loops^{63–65} are also worthy of note. Meanwhile, it is worth studying that exploring higher-order topological states through different mechanisms, for example, systems with defect modes^{66,67}.

The above investigations only focus on the case of 3D HOTIs. In fact, the research methods can also be extended to systems larger than three dimensions. It has been confirmed that the higher-dimensional systems possess some properties that their lower-dimensional counterparts do not support, such as four-dimensional quantum Hall effect^{68,69}, Yang monopoles⁷⁰, 2D Weyl surfaces in five-dimensional systems⁷¹ and so on. If the non-Abelian gauge potentials are introduced into these high-dimensional systems, what novel phenomena will occur is very worth exploring. In addition, our studies also imply novel ways to control electrical signals, and may have potential applications in the field of electronic signal control.

Methods

Synchronization between real-space motion and band-population dynamics. Here, we give an elucidation on the synchronization between real-space and band-population dynamics with the atomic limit $J_2 = 0$, where we study the time dynamics of a single unit cell. The lowest energy eigenstates are given as

$$\begin{aligned} |\psi^1\rangle &= (0, 1/\sqrt{6}, 1/\sqrt{6}, -1/\sqrt{6}, 0, 0, 0, 1/\sqrt{2})^T, \\ |\psi^2\rangle &= (-1/\sqrt{6}, 0, -1/\sqrt{6}, -1/\sqrt{6}, 0, 0, 1/\sqrt{2}, 0)^T, \\ |\psi^3\rangle &= (1/\sqrt{6}, -1/\sqrt{6}, 0, -1/\sqrt{6}, 0, 1/\sqrt{2}, 0, 0)^T, \\ |\psi^4\rangle &= (-1/\sqrt{6}, -1/\sqrt{6}, 1/\sqrt{6}, 0, 1/\sqrt{2}, 0, 0, 0)^T. \end{aligned} \quad (3)$$

By setting the spatial origin at the plaquette center, we can construct the position operator $\hat{\mathbf{r}} = \sum_i (\mathbf{r}_i - \mathbf{r}_0) |\mathbf{r}_i\rangle \langle \mathbf{r}_i|$, whose components on three directions are the matrices

$$\begin{aligned} \hat{x} &= \text{diag}(-1/2, -1/2, 1/2, 1/2, -1/2, -1/2, 1/2, 1/2)\delta, \\ \hat{y} &= \text{diag}(1/2, -1/2, 1/2, -1/2, 1/2, -1/2, 1/2, -1/2)\delta, \\ \hat{z} &= \text{diag}(-1/2, 1/2, 1/2, -1/2, 1/2, -1/2, -1/2, 1/2)\delta. \end{aligned} \quad (4)$$

Then we construct the projected position operators $\hat{r}_{P,i} = \hat{P} \hat{r}_i \hat{P} = \sum_{\alpha,\beta=1}^4 |\psi^\alpha\rangle \langle \psi^\alpha| \hat{r}_i |\psi^\beta\rangle \langle \psi^\beta|$ for $i = x, y, z$, with $\hat{P} = \sum_{\alpha=1}^4 |\psi^\alpha\rangle \langle \psi^\alpha|$. Notice that there is $[\hat{r}_i, \hat{r}_j] \neq 0$ when $i \neq j$. Given an applied force \mathbf{F} , the perturbative Hamiltonian governing the dynamics reads

$$\begin{aligned} \hat{H}_F &= \mathbf{F} \cdot \hat{\mathbf{r}}_P = \sum_{i=x,y,z} F_i \hat{r}_{P,i} \\ &= \frac{\delta}{3} \begin{pmatrix} F_x - F_y + F_z & (-F_y - F_z)/2 & (F_x - F_z)/2 & (F_x + F_y)/2 \\ (-F_y - F_z)/2 & F_x + F_y - F_z & (F_x - F_y)/2 & (-F_x - F_z)/2 \\ (F_x - F_z)/2 & (F_x - F_y)/2 & -F_x - F_y - F_z & (-F_y + F_z)/2 \\ (F_x + F_y)/2 & (-F_x - F_z)/2 & (-F_y + F_z)/2 & -F_x + F_y + F_z \end{pmatrix}. \end{aligned} \quad (5)$$

Starting with the initial state $|\psi_{\mathbf{k}}(0)\rangle = \eta_1(0)|\psi_{\mathbf{k}}^1\rangle + \eta_2(0)|\psi_{\mathbf{k}}^2\rangle + \eta_3(0)|\psi_{\mathbf{k}}^3\rangle + \eta_4(0)|\psi_{\mathbf{k}}^4\rangle$, the evolution results of the wavepacket can be expressed as the solution of the Schrodinger's equation as $|\psi_{\mathbf{k}}(t)\rangle = U(t)|\psi_{\mathbf{k}}(0)\rangle$, where the evolution operator reads $U(t) = e^{-i\hat{H}_F t}$. Let us focus on the dynamics along path L_1 , where $F_x = F_y = F_z$. The evolution operator can be expressed as

$$U_{C_1}(t) = \frac{1}{3} \begin{pmatrix} 2 + e^{-i\delta F_x t} & 1 - e^{-i\delta F_x t} & 0 & -1 + e^{-i\delta F_x t} \\ 1 - e^{-i\delta F_x t} & 2 + e^{-i\delta F_x t} & 0 & 1 - e^{-i\delta F_x t} \\ 0 & 0 & 3e^{i\delta F_x t} & 0 \\ -1 + e^{-i\delta F_x t} & 1 - e^{-i\delta F_x t} & 0 & 2 + e^{-i\delta F_x t} \end{pmatrix}. \quad (6)$$

We can calculate the time-dependent coefficients $\eta_i(t)$ as

$$\begin{aligned} \eta_1(t) &= \frac{1}{3} [2\eta_1(0) + \eta_2(0) - \eta_4(0) + e^{-i\delta F_x t} (\eta_1(0) - \eta_2(0) + \eta_4(0))], \\ \eta_2(t) &= \frac{1}{3} [\eta_1(0) + 2\eta_2(0) - \eta_4(0) + e^{-i\delta F_x t} (-\eta_1(0) + \eta_2(0) - \eta_4(0))], \\ \eta_3(t) &= e^{i\delta F_x t} \eta_3(0), \\ \eta_4(t) &= \frac{1}{3} [-\eta_1(0) + \eta_2(0) + 2\eta_4(0) + e^{-i\delta F_x t} (\eta_1(0) - \eta_2(0) + \eta_4(0))]. \end{aligned} \quad (7)$$

It can be seen that the band populations can be expressed as

$$|\eta_i(t)|^2 = M_i^2 + N_i^2 + 2M_i N_i \cos(\delta F_x t), \quad (8)$$

for $i = 1, 2, 4$, where M_i and N_i are constant coefficients consisting of $\eta_1(0)$, $\eta_2(0)$, and $\eta_4(0)$. As a result, the band populations $|\eta_i(t)|^2$ experience cosine oscillations with a period $2\pi/(\delta|F_x|)$ except for $|\eta_3(t)|^2$, which remains unchanged. Meanwhile, the period for the BO along the body diagonal is $T_B = |\mathbf{G}|/|\mathbf{F}| = \pi/(\delta|F_x|)$, which is half of that for the band-population dynamics. The synchronization along the other three paths can also be demonstrated.

Furthermore, the perturbative Hamiltonian in Eq. (5) has four levels read as $E_{F,1} = \frac{\delta}{\sqrt{6}} \sqrt{F^2 + \sqrt{3}\Theta}$, $E_{F,2} = \frac{\delta}{\sqrt{6}} \sqrt{F^2 - \sqrt{3}\Theta}$, $E_{F,3} = -\frac{\delta}{\sqrt{6}} \sqrt{F^2 - \sqrt{3}\Theta}$ and $E_{F,4} = -\frac{\delta}{\sqrt{6}} \sqrt{F^2 + \sqrt{3}\Theta}$, where $F^2 = \sum_i F_i^2$ and $\Theta = \sum_{i \neq j} F_i^2 F_j^2$ for $i, j = x, y, z$. The interband transitions occurs in the form of a Rabi oscillation between any two of the levels with a period of $T_R = 2\pi/\Delta E$, where ΔE can be the difference between any two of the levels. Since there are four levels, a period evolution can only exist when there is a common multiple period T_{CM} for all these Rabi periods. However, along other symmetry axis, such T_{CM} does not exist. Therefore, in this 3D system, topological BO phenomena can only occur along the body diagonals.

Correspondence between the designed circuit and the 3D lattice model. Here, we give a detailed demonstration on the circuit design, which corresponds to the time-dependent Schrödinger equation for the real-space wavepacket. According to the circuit structure given in Fig. 2a~e, where two circuit nodes are used to simulate one lattice site, the evolution of the voltages at each node a_{\pm} can be written as a set of differential equations through Kirchhoff's current law, as

$$C_{a_{\pm}} \frac{dV_{a_{\pm}}}{dt} + \frac{V_{a_{\pm}}}{R_{a_{\pm}}} = \sum_b \frac{V_{b_{\mp}} - V_{a_{\pm}}}{R_{a_{\pm} b_{\mp}}} \quad (9)$$

where b includes all the sites connected to site a and a itself. Here, the two terms on the left of the equations are the contribution of the grounding capacitors and grounding resistors to the currents flowing away from nodes a_{\pm} to the ground, respectively, and the terms on the right are the currents flowing into nodes a_{\pm} from other nodes. These differential equations can be written in the form of a Schrödinger-like equation $i\partial_t |\phi(t)\rangle = H_e |\phi(t)\rangle$, where $|\phi(t)\rangle$ is the circuit state consisting of voltages of $2n$ nodes, as

$$|\phi(t)\rangle = (V_{1_+}(t), V_{2_+}(t), \dots, V_{n_+}(t), V_{1_-}(t), V_{2_-}(t), \dots, V_{n_-}(t))^T \quad (10)$$

and the circuit Hamiltonian H_e are consisting of the circuit components and can be written in the form of a partitioned matrix, as

$$H_e = i \begin{pmatrix} Y_{1+} & & & C_{1+}^{-1}R_{1+1-}^{-1} & C_{1+}^{-1}R_{1+2-}^{-1} & \cdots \\ & \cdots & & C_{2+}^{-1}R_{2+1-}^{-1} & \cdots & \cdots \\ & & Y_{n+} & \cdots & \cdots & C_{n+}^{-1}R_{n+n-}^{-1} \\ \cdots & C_{1-}^{-1}R_{1-1+}^{-1} & C_{1-}^{-1}R_{1-2+}^{-1} & \cdots & Y_{1-} & \\ \cdots & C_{2-}^{-1}R_{2-1+}^{-1} & \cdots & \cdots & \cdots & \\ \cdots & \cdots & \cdots & C_{n-}^{-1}R_{n-n+}^{-1} & \cdots & Y_{n-} \end{pmatrix} \quad (11)$$

$$= \begin{pmatrix} H_{11} & H_{12} \\ H_{21} & H_{22} \end{pmatrix},$$

where the diagonal elements are expressed as $Y_{a_{\pm}} = iC_{a_{\pm}}^{-1}(-R_{a_{\pm}}^{-1} - \sum_b R_{a_{\pm}b_{\pm}}^{-1})$, and all the submatrices have a size of $n \times n$. Our goal is to construct the matrix $H_e =$

$i \begin{pmatrix} O & -H_B' \\ H_B' & O \end{pmatrix}$ through appropriate settings of the circuit components, where H_B' corresponds to the real-space Hamiltonian H_B for the 3D lattice model.

We first determine the capacitances. We have $C_{a_+}^{-1}R_{a_+b_+}^{-1} = C_{b_+}^{-1}R_{b_+a_+}^{-1}$, since H_B is Hermitian. Then, according to $H_{12} = -H_{21}$, we have $C_{a_+}^{-1}R_{a_+b_+}^{-1} = -C_{a_-}^{-1}R_{a_-b_+}^{-1} = C_{a_-}^{-1}R_{b_+a_-}^{-1}$. Here, the relationship $R_{a_+b_+} = -R_{b_+a_+}$ is naturally established due to the properties of INIC. Combining the above equations, we can conclude that $C_{a_+} = C_{b_+}$ is established for any nodes a and b . Thus, we set all the capacitances to C_0 . Then, the effective resistances of the INICs are determined so that each element in the submatrix H_{21} corresponds to that in H_B , that is, $R_{a_-b_+} = C_0^{-1}(H_B^{ab})^{-1}$. Moreover, we choose appropriate grounding resistances to construct the zero diagonal elements in H_{11} and H_{22} , which is $R_{a_{\pm}} = -(\sum_b R_{a_{\pm}b_{\pm}}^{-1})^{-1}$. Notice that the resistance $R_{a_{\pm}}$ might be positive or negative that should be fulfilled through a normal resistor or an INIC with effective resistance of $|R_{a_{\pm}}|$, respectively.

To demonstrate the topological BOs, the circuit state evolves as the solution of the Schrödinger-like equation, as $|\phi(t)\rangle = e^{-iH_e t}|\phi(0)\rangle$, where the initial state is set as $|\phi(0)\rangle = (\text{Re}(|\psi(0)\rangle), -\text{Im}(|\psi(0)\rangle))^T$. Here, $|\psi(0)\rangle$ corresponds to the initial lattice wavepacket $|\psi(0)\rangle$ in real space and $|\psi_{r,\mu}(t=0)\rangle = |\psi_{l,\mu}^1\rangle$, where μ indicates the sublattice degree of freedom in the unit cell. Considering the example we take in the main text, the initial voltages are set to (0, 1, 1, -1, 0, 0, 0, 1.73) V for the real nodes in each unit cells and 0 V for the imaginary nodes for convenience. The solution can be calculated as

$$\begin{aligned}
|\phi(t)\rangle &= \begin{pmatrix} \cos(H_B' t) & -\sin(H_B' t) \\ \sin(H_B' t) & \cos(H_B' t) \end{pmatrix} \begin{pmatrix} \text{Re}(|\psi(0)\rangle) \\ -\text{Im}(|\psi(0)\rangle) \end{pmatrix} \\
&= \begin{pmatrix} \cos(H_B' t)\text{Re}(|\psi(0)\rangle) + \sin(H_B' t)\text{Im}(|\psi(0)\rangle) \\ \sin(H_B' t)\text{Re}(|\psi(0)\rangle) - \cos(H_B' t)\text{Im}(|\psi(0)\rangle) \end{pmatrix}. \quad (12)
\end{aligned}$$

We define $|\psi(t)\rangle$ as the projection of $|\phi(t)\rangle$ on $(1 \ -i) \otimes I_N$, namely

$$\begin{aligned}
|\psi(t)\rangle &= (1 \ -i) \otimes I_N |\phi(t)\rangle \\
&= (\cos(H_B' t) - i \sin(H_B' t))(\text{Re}(|\psi(0)\rangle) + i\text{Im}(|\psi(0)\rangle)) \quad (13) \\
&= e^{-iH_B' t} |\psi(0)\rangle,
\end{aligned}$$

which corresponds to the evolution results in the lattice model.

Notice that $|\psi(t)\rangle$ can also be expressed as a recombination of the circuit voltages, as

$$\begin{aligned}
|\psi(t)\rangle &= (1 \ -i) \otimes I_N |\phi(t)\rangle \\
&= \begin{pmatrix} V_{1+}(t) - iV_{1-}(t) \\ V_{2+}(t) - iV_{2-}(t) \\ \vdots \\ V_{n+}(t) - iV_{n-}(t) \end{pmatrix} = \begin{pmatrix} v_1(t) \\ v_2(t) \\ \vdots \\ v_n(t) \end{pmatrix} \quad (14)
\end{aligned}$$

which demonstrates that one site in the lattice model can be exactly formed by two circuit nodes.

It is worthy to note that since the circuit Hamiltonian satisfies $H_e = \sigma_2 \otimes H_B'$, it can be demonstrated that H_e satisfies the same symmetries with H_B' . That is, if H_B' satisfies the symmetry Θ under operator X , where $XH_B'X^{-1} = \Theta(H_B')$, there exists $X_e = \sigma_2 \otimes X$ making $X_e H_e X_e^{-1} = \Theta(H_e)$. Thus, our designed circuit is an effective correspondence to the lattice model.

Data availability

All data that support the findings in this study are displayed in the main text and Supplementary Information.

Code availability

The code that supports the plots within this paper is available from the corresponding author upon reasonable request.

Received: 26 June 2023; Accepted: 17 November 2023;

Published online: 06 December 2023

References

- Hasan, M. Z. & Kane, C. L. Colloquium: Topological insulators. *Rev. Mod. Phys.* **82**, 3045–3067 (2010).

2. Qi, X.-L. & Zhang, S.-C. Topological insulators and superconductors. *Rev. Mod. Phys.* **83**, 1057–1110 (2011).
3. Lu, L., Joannopoulos, J. D. & Soljačić, M. Topological photonics. *Nat. Photonics* **8**, 821–829 (2014).
4. Ozawa, T. et al. Topological photonics. *Rev. Mod. Phys.* **91**, 015006 (2019).
5. Ma, G., Meng, X. & Chan, C. T. Topological phases in acoustic and mechanical systems. *Nat. Rev. Phys.* **1**, 281–294 (2019).
6. Nayak, C., Simon, S. H., Stern, A., Freedman, M. & Das Sarma, S. Non-abelian anyons and topological quantum computation. *Rev. Mod. Phys.* **80**, 1083–1159 (2008).
7. Pachos, J. K. *Introduction to Topological Quantum Computation* (Cambridge University Press, Cambridge, England, 2012).
8. Chiu, C.-K., Teo, J. C. Y., Schnyder, A. P. & Ryu, S. Classification of topological quantum matter with symmetries. *Rev. Mod. Phys.* **88**, 035005 (2016).
9. Bouhon, A. et al. Non-Abelian reciprocal braiding of Weyl points and its manifestation in ZrTe. *Nat. Phys.* **16**, 1137–1143 (2020).
10. Jiang, B. et al. Experimental observation of non-Abelian topological acoustic semimetals and their phase transitions. *Nat. Phys.* **17**, 1239–1246 (2021).
11. Benalcazar, W. A., Bernevig, B. A. & Hughes, T. L. Quantized electric multipole insulators. *Science* **357**, 61–66 (2017).
12. Serra-García, M. et al. Observation of a phononic quadrupole topological insulator. *Nature* **555**, 342–345 (2018).
13. Peterson, C., Benalcazar, W., Hughes, T. & Bahl, G. A quantized microwave quadrupole insulator with topologically protected corner states. *Nature* **555**, 346–350 (2018).
14. Xue, H., Yang, Y., Gao, F., Chong, Y. & Zhang, B. Acoustic higher-order topological insulator on a kagome lattice. *Nat. Mater.* **18**, 108–112 (2019).
15. Zhang, X. et al. Second-order topology and multidimensional topological transitions in sonic crystals. *Nat. Phys.* **15**, 582–588 (2019).
16. Ni, X., Weiner, M., Alù, A. & Khanikaev, A. B. Observation of higher-order topological acoustic states protected by generalized chiral symmetry. *Nat. Mater.* **18**, 113–120 (2019).
17. Noh, J. et al. Topological protection of photonic mid-gap defect modes. *Nat. Photonics* **12**, 408 (2018).
18. Mittal, S. et al. Photonic quadrupole topological phases. *Nat. Photonics* **13**, 692–696 (2019).
19. Xie, B. Y. et al. Visualization of higher-order topological insulating phases in two-dimensional dielectric photonic crystals. *Phys. Rev. Lett.* **122**, 233903 (2019).
20. Chen, X. D. et al. Direct observation of corner states in second-order topological photonic crystal slabs. *Phys. Rev. Lett.* **122**, 233902 (2019).
21. Peterson, C. W., Li, T., Benalcazar, W. A., Hughes, T. L. & Bahl, G. A fractional corner anomaly reveals higher-order topology. *Science* **368**, 1114–1118 (2020).
22. Liu, Y. et al. Bulk–disclination correspondence in topological crystalline insulators. *Nature* **589**, 381–385 (2021).
23. Schindler, F. et al. Higher-order topology in bismuth. *Nat. Phys.* **14**, 918–924 (2018).
24. Imhof, S. et al. Topoelectrical-circuit realization of topological corner modes. *Nat. Phys.* **14**, 925–929 (2018).
25. Bao, J. et al. Topoelectrical circuit octupole insulator with topologically protected corner states. *Phys. Rev. B* **100**, 201406(R) (2019).
26. Feldmann, J. et al. Optical investigation of Bloch oscillations in a semiconductor superlattice. *Phys. Rev. B* **46**, 7252(R) (1992).
27. Waschke, C. et al. Coherent submillimeter-wave emission from Bloch oscillations in a semiconductor superlattice. *Phys. Rev. Lett.* **70**, 3319 (1993).
28. Ben Dahan, M., Peik, E., Reichel, J., Castin, Y. & Salomon, C. Bloch oscillations of atoms in an optical potential. *Phys. Rev. Lett.* **76**, 4508–4511 (1996).
29. Wilkinson, S. R., Bharucha, C. F., Madison, K. W., Niu, Q. & Raizen, M. G. Observation of atomic Wannier Stark ladders in an accelerating optical potential. *Phys. Rev. Lett.* **76**, 4512 (1996).
30. Anderson, B. P. & Kasevich, M. A. Macroscopic quantum interference from atomic tunnel arrays. *Science* **282**, 1686–1689 (1998).
31. Morsch, O., Müller, J. H., Cristiani, M., Ciampini, D. & Arimondo, E. Bloch oscillations and mean-field effects of Bose-Einstein condensates in 1D optical lattices. *Phys. Rev. Lett.* **87**, 140402 (2001).
32. Morandotti, R., Peschel, U., Aitchison, J. S., Eisenberg, H. S. & Silberberg, Y. Experimental observation of linear and nonlinear optical Bloch oscillations. *Phys. Rev. Lett.* **83**, 4756–4759 (1999).
33. Lenz, G., Talanina, I. & Martijn de Sterke, C. Bloch oscillations in an array of curved optical waveguides. *Phys. Rev. Lett.* **83**, 963–966 (1999).
34. Pertsch, T., Dannberg, P., Elflein, W., Bräuer, A. & Lederer, F. Optical Bloch oscillations in temperature tuned waveguide arrays. *Phys. Rev. Lett.* **83**, 4752–4755 (1999).
35. Sapienza, R. et al. Optical analogue of electronic Bloch oscillations. *Phys. Rev. Lett.* **91**, 263902 (2003).
36. Dreisow, F. et al. Bloch-Zener oscillations in binary superlattices. *Phys. Rev. Lett.* **102**, 076802 (2009).
37. Corrielli, G., Crespi, A., Della Valle, G., Longhi, S. & Osellame, R. Fractional Bloch oscillations in photonic lattices. *Nat. Commun.* **4**, 1555 (2013).
38. Liu, X.-J., Law, K. T., Ng, T. K. & Lee, P. A. Detecting topological phases in cold atoms. *Phys. Rev. Lett.* **111**, 120402 (2013).
39. Block, A. et al. Bloch oscillations in plasmonic waveguide arrays. *Nat. Commun.* **5**, 3483 (2014).
40. Xu, Y. L. et al. Experimental realization of Bloch oscillations in a parity-time synthetic silicon photonic lattice. *Nat. Commun.* **7**, 11319 (2016).
41. Meinert, F. et al. Bloch oscillations in the absence of a lattice. *Science* **356**, 945 (2017).
42. Reislöhner, J. et al. Onset of Bloch oscillations in the almost-strong-field regime. *Nat. Commun.* **13**, 7716 (2022).
43. Li, T. et al. Schneider, Bloch state tomography using Wilson lines. *Science* **352**, 1094 (2016).
44. Höller, J. & Alexandradinata, A. Topological Bloch oscillations. *Phys. Rev. B* **98**, 024310 (2018).
45. Di Liberto, M., Goldman, N. & Palumbo, G. Non-Abelian Bloch oscillations in higher-order topological insulators. *Nat. Commun.* **11**, 5942 (2020).
46. Xiao, D., Chang, M. C. & Niu, Q. Berry phase effects on electronic properties. *Rev. Mod. Phys.* **82**, 1959 (2010).
47. Surl, S., Tyner, A. C. & Goswami, P. Mixed-order topology of Benalcazar-Bernevig-Hughes models. Preprint at <https://arxiv.org/abs/2201.07205> (2022).
48. Albert, V. V., Glazman, L. I. & Jiang, L. Topological properties of linear circuit lattices. *Phys. Rev. Lett.* **114**, 173902 (2015).
49. Ning, J., Owens, C., Sommer, A., Schuster, D. & Simon, J. Time and site resolved dynamics in a topological circuit. *Phys. Rev. X* **5**, 021031 (2015).
50. Lee, C. H. et al. Topoelectrical circuits. *Commun. Phys.* **1**, 39 (2018).
51. Hofmann, T., Helbig, T., Lee, C., Greiter, M. & Thomale, R. Chiral voltage propagation and calibration in a topoelectrical Chern circuit. *Phys. Rev. Lett.* **122**, 247702 (2019).
52. Li, L., Lee, C. & Gong, J. Emergence and full 3D-imaging of nodal boundary Seifert surfaces in 4D topological matter. *Commun. Phys.* **2**, 135 (2019).
53. Helbig, T. et al. Generalized bulk–boundary correspondence in non-Hermitian topoelectrical circuits. *Nat. Phys.* **16**, 747 (2020).
54. Wang, Y., Price, H. M., Zhang, B. & Chong, Y. D. Circuit implementation of a four-dimensional topological insulator. *Nat. Commun.* **11**, 2356 (2020).
55. Olekhno, N. A. et al. Topological edge states of interacting photon pairs emulated in a topoelectrical circuit. *Nat. Commun.* **11**, 1436 (2020).
56. Zhang, W. et al. Experimental observation of higher-order topological Anderson insulators. *Phys. Rev. Lett.* **126**, 146802 (2021).
57. Pan, N., Chen, T., Sun, H. & Zhang, X. Electric-circuit realization of fast quantum search. *Research* 9793071 (2021).
58. Zhang, W., Yuan, H., Sun, N., Sun, H. & Zhang, X. Observation of novel topological states in hyperbolic lattices. *Nat. Commun.* **13**, 2937 (2022).
59. Zhang, W. et al. Observation of Bloch oscillations dominated by effective anyonic particle statistics. *Nat. Commun.* **13**, 2392 (2022).
60. Wu, J. et al. Non-Abelian gauge fields in circuit systems. *Nat. Electron.* **10**, 1038 (2022).
61. Zhu, P., Sun, X. Q., Hughes, T. L. & Bahl, G. Higher rank chirality and non-Hermitian skin effect in a topoelectrical circuit. *Nat. Commun.* **14**, 720 (2023).
62. Zhang, W., Di, F., Zheng, X., Sun, H. & Zhang, X. Hyperbolic band topology with non-trivial second Chern numbers. *Nat. Commun.* **14**, 1083 (2023).
63. Kruthoff, J., de Boer, J., van Wezel, J., Kane, C. L. & Slager, R.-J. Topological classification of crystalline insulators through band structure combinatorics. *Phys. Rev. X* **7**, 041069 (2017).
64. Po, H. C., Vishwanath, A. & Watanabe, H. Symmetry-based indicators of band topology in the 230 space groups. *Nat. Commun.* **8**, 50 (2017).
65. Bouhon, A., Black-Schaffer, A. M. & Slager, R.-J. Wilson loop approach to fragile topology of split elementary band representations and topological crystalline insulators with time-reversal symmetry. *Phys. Rev. B* **100**, 195135 (2019).
66. Slager, R. J., Rademaker, L., Zaane, J. & Balents, L. Impurity-bound states and Green’s function zeros as local signatures of topology. *Phys. Rev. B* **92**, 085126 (2015).
67. Ran, Y., Zhang, Y. & Vishwanath, A. One-dimensional topologically protected modes in topological insulators with lattice dislocations. *Nat. Phys.* **5**, 298–303 (2009).
68. Lohse, M., Schweizer, C., Price, H. M., Zilberberg, O. & Bloch, I. Exploring 4D quantum Hall physics with a 2D topological charge pump. *Nature* **553**, 55–58 (2018).
69. Zilberberg, O. et al. Photonic topological boundary pumping as a probe of 4D quantum Hall physics. *Nature* **553**, 59–62 (2018).
70. Sugawa, S., Salces-Carcoba, F., Perry, A. R., Yue, Y. & Spielman, I. B. Second Chern number of a quantum-simulated non-Abelian Yang monopole. *Science* **360**, 1429–1434 (2018).

71. Ma, S. et al. Linked Weyl surfaces and Weyl arcs in photonic metamaterials. *Science* **373**, 572–576 (2021).

Acknowledgements

This work was supported by the National Key R & D Program of China under Grant No. 2017YFA0303800 and the National Natural Science Foundation of China (91850205).

Author contributions

T.C. finished the theoretical investigation on Topological BOs and higher-order topological states with the help of N.P. N.P. finished the experiments with the help of T.J. and X.T. N.P., T.C., and X.Z. wrote the paper. X.Z. initiated and designed this research project.

Competing interests

The authors declare no competing interests.

Additional information

Supplementary information The online version contains supplementary material available at <https://doi.org/10.1038/s42005-023-01474-9>.

Correspondence and requests for materials should be addressed to Tian Chen or Xiangdong Zhang.

Peer review information *Communications Physics* thanks the anonymous reviewers for their contribution to the peer review of this work. A peer review file is available.

Reprints and permission information is available at <http://www.nature.com/reprints>

Publisher's note Springer Nature remains neutral with regard to jurisdictional claims in published maps and institutional affiliations.



Open Access This article is licensed under a Creative Commons Attribution 4.0 International License, which permits use, sharing, adaptation, distribution and reproduction in any medium or format, as long as you give appropriate credit to the original author(s) and the source, provide a link to the Creative Commons licence, and indicate if changes were made. The images or other third party material in this article are included in the article's Creative Commons licence, unless indicated otherwise in a credit line to the material. If material is not included in the article's Creative Commons licence and your intended use is not permitted by statutory regulation or exceeds the permitted use, you will need to obtain permission directly from the copyright holder. To view a copy of this licence, visit <http://creativecommons.org/licenses/by/4.0/>.

© The Author(s) 2023